Supplementary Information for:
Chiral-angle-selected spin splitting and spin-polarized conduction in nanotubes rolled from d-wave altermagnets

Ersoy Şaşıoğlu[1], Tom G. Saunderson[1], Börge Göbel[1], Ingrid Mertig[1], and Samir Lounis[1]

[1] *Institute of Physics and Halle-Berlin-Regensburg Cluster of Excellence CCE, Martin Luther University Halle-Wittenberg, 06120 Halle (Saale), Germany*

The Supplementary Information provides further details on the tight-binding model and first-principles calculations underlying the results presented in the main text. In particular, it documents the tight-binding parameters used in the calculations of Fig. 1 of the main text, the construction of nanotube geometries from two-dimensional altermagnetic parent materials, and the computational methodology employed in the density-functional-theory calculations. The Supplementary Information further discusses experimentally motivated material platforms, including layered altermagnets and recently proposed monolayer altermagnetic materials, and presents a representative set of candidate altermagnetic and Janus altermagnetic monolayers for nanotube realization. Additional electronic-structure results are provided for nanotubes rolled from V_2OSe_2, V_2OSeTe, and Fe_2SSe, together with an analysis of residual magnetic moments as a function of nanotube radius. These results further support the chiral-angle-selected spin splitting established in the main text and demonstrate its robustness across the representative nanotube systems considered here.

DETAILS OF THE TIGHT-BINDING CALCULATIONS

The tight-binding calculations shown in Fig. 1 of the main text were performed using the minimal two-sublattice Hamiltonian introduced in the main text,

$$H_\sigma(\mathbf{k}) = \varepsilon(\mathbf{k})\tau_0 + t_{AB}(\mathbf{k})\tau_x + \left[J\sigma + \lambda g_d(\mathbf{k})\right]\tau_z, \tag{1}$$

with

$$\varepsilon(\mathbf{k}) = -2t_0(\cos k_x + \cos k_y), \tag{2}$$

$$t_{AB}(\mathbf{k}) = -4t_1 \cos\frac{k_x}{2}\cos\frac{k_y}{2}, \tag{3}$$

and

$$g_d(\mathbf{k}) = \cos k_x - \cos k_y. \tag{4}$$

The numerical parameters used throughout Fig. 1 of the main text were

$$t_0 = 0.85, \qquad t_1 = 0.28, \qquad J = 0.55, \qquad \lambda = 0.55, \qquad \mu = -1.55, \tag{5}$$

where t_0 denotes the intra-sublattice hopping amplitude, t_1 the inter-sublattice hybridization, J the staggered exchange field, λ the strength of the d-wave altermagnetic spin splitting, and μ the chemical potential shift. These parameters were chosen to produce a metallic parent altermagnet with a pronounced momentum-dependent spin splitting in the vicinity of the Fermi level.

The two-dimensional band structure in Fig. 1(a) was calculated along the high-symmetry path $X - \Gamma - Y$ of the square-lattice Brillouin zone. The nanotube band structures shown in Figs. 1(c)–1(e) were obtained by introducing rotated momentum coordinates,

$$k_x = k_\parallel \cos\theta - k_\perp \sin\theta, \tag{6}$$

$$k_y = k_\parallel \sin\theta + k_\perp \cos\theta, \tag{7}$$

together with the quantized transverse momentum

$$k_\perp = \frac{2\pi n}{C}, \tag{8}$$

where $C = 8$ denotes the dimensionless nanotube circumference used in the illustrative calculations and $n = 0, 1, 2$ labels the transverse subbands included in Fig. 1. The precise value of C is not essential for the chiral-angle dependence discussed in the main text and primarily controls the spacing between neighboring subbands.

Figures 1(c)–1(e) display the low-energy nanotube subband structures obtained from the transverse modes $n = 0, 1, 2$ for chiral angles $\theta = 0°$, $45°$, and $90°$, respectively. The resulting electronic structures capture the characteristic antinodal–nodal distinction discussed in the main text: the antinodal nanotubes exhibit spin splitting, whereas the complete spectrum of the nodal nanotube is spin degenerate. For the $n = 0$ mode, corresponding to $k_\perp = 0$, the spin splitting exhibits the $\cos(2\theta)$ scaling derived in the main text. For the $n \neq 0$ modes, additional terms arising from finite $k_\perp$ contribute, and no universal $\cos(2\theta)$ dependence is expected.

The purpose of this minimal model is not to reproduce the electronic structure of a specific material quantitatively, but rather to isolate the symmetry and geometrical ingredients underlying the chiral-angle-selected spin splitting inherited from the parent d-wave electronic structure. As shown in the main text, first-principles calculations for V_2O and other representative nanotubes rolled from 2D d-wave altermagnets reproduce the same characteristic antinodal–nodal distinction predicted by the tight-binding model.

COMPUTATIONAL DETAILS

First-principles calculations were performed within density-functional theory using the generalized gradient approximation (GGA) in the Perdew–Burke–Ernzerhof (PBE) parametrization for the exchange–correlation functional. All calculations were carried out using the QuantumATK package employing norm-conserving PseudoDojo pseudopotentials and LCAO basis sets [1–3].

The electronic structures of the checkerboard V_2O monolayer and the corresponding nanotube geometries were investigated within collinear antiferromagnetic order. The primitive V_2O monolayer contains two magnetic V sublattices arranged in a checkerboard configuration, giving rise to the d-wave altermagnetic spin splitting discussed in the main text. Structural relaxations were performed until the residual atomic forces were smaller than 0.01 eV/Å. The optimized lattice constant of the V_2O monolayer is $a = 3.85$ Å.

Nanotube geometries were constructed from commensurate supercells of the parent V_2O monolayer corresponding to the desired chiral angles θ. For the achiral antinodal nanotubes ($\theta = 0°$ and $90°$), the nanotube unit cells were generated from 1×18 rectangular supercells of the primitive V_2O monolayer. For the achiral nodal configuration ($\theta = 45°$), a $\sqrt{2} \times \sqrt{2}$ tetragonal cell was first constructed from the primitive cell, followed by the generation of a 1×13 supercell prior to rolling.

For the intermediate chiral nanotubes used in the transport calculations, rotated $\sqrt{5}\times\sqrt{5}$ and $\sqrt{10}\times\sqrt{10}$ square cells were constructed for $\theta \simeq 27°$ and $\simeq 18°$, respectively. These cells were subsequently transformed into commensurate 2D tetragonal supercells and rolled into the corresponding nanotube geometries. These structures provide intermediate chiral angles between the achiral antinodal ($\theta = 0°$) and nodal ($\theta = 45°$) limits considered in the transport calculations.

For the achiral geometries used to compare the zone-folded electronic structure before and after rolling, the corresponding 2D supercells contain the same number of atoms as the resulting nanotube unit cells, enabling direct comparison between the unrolled-supercell and nanotube electronic structures discussed in the main text. A vacuum separation larger than 20 Å was used between periodic images along the directions perpendicular to the nanotube axis.

Brillouin-zone integrations for the monolayers employed Monkhorst–Pack k-point meshes of $20 \times 20 \times 1$, while nanotube calculations used one-dimensional k-point grids equivalent to at least 20 k points along the nanotube Brillouin zone. Electronic band structures were calculated along the X–Γ–Y path for the primitive monolayers, along the Γ–X direction for the corresponding rectangular supercells, and along the nanotube Γ–Z direction for the one-dimensional nanotube geometries. Additional calculations were performed for the circumferential nanotube states and the corresponding long-direction supercell bands discussed in Fig. S1.

In addition to the V_2O system discussed in the main text, further calculations were performed for representative symmetric and Janus monolayers, including V_2OSe_2, V_2OSeTe, and Fe_2SSe. For each system, nanotubes with three different radii were constructed using the same computational framework, enabling a systematic analysis of the radius dependence of the residual magnetic moment. The resulting electronic structures and magnetic moments were used

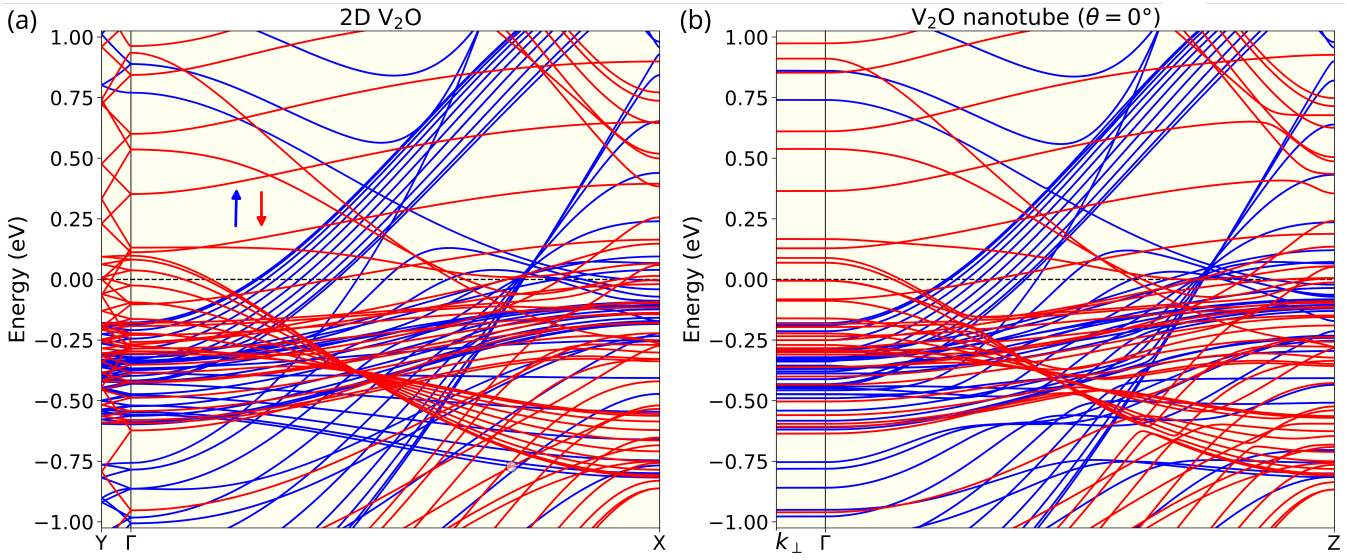


FIG. S1. Zone folding and circumferential quantization in a V_2O nanotube. (a) Electronic structure of the 1×18 rectangular supercell of checkerboard V_2O calculated along the long-direction Y–Γ and short-direction Γ–X paths. (b) Electronic structure of the corresponding $\theta = 0°$ V_2O nanotube, showing the circumferential states associated with quantized $k_\perp$ and the dispersive nanotube bands along the Γ–Z axis.

to assess the robustness of the chiral-angle-selected spin splitting against material-dependent structural and magnetic changes induced by rolling.

ZONE FOLDING AND CIRCUMFERENTIAL QUANTIZATION

Before discussing representative material candidates, we further illustrate how the electronic structure of the parent 2D V_2O layer is transformed upon rolling. Figure S1 compares the electronic structure of the 1×18 unrolled rectangular supercell of 2D V_2O with that of the corresponding $\theta = 0°$ nanotube. While Fig. 3 of the main text focuses on the correspondence between the supercell Γ–X dispersion and the nanotube Γ–Z dispersion along the tube axis, Fig. S1 additionally shows the electronic structure along the long direction of the rectangular supercell and the corresponding circumferential states of the nanotube.

Along the short direction of the unrolled rectangular supercell, the zone-folded electronic structure closely resembles the dispersive nanotube bands along the tube axis. This correspondence shows that the characteristic spin-split 1D bands are already encoded in the zone-folded electronic structure of the parent 2D layer before rolling. Along the long direction, the unrolled supercell retains a continuous dispersion, whereas rolling imposes periodic boundary conditions around the nanotube circumference and quantizes the corresponding transverse momentum. The transverse electronic structure is therefore represented by discrete circumferential subbands rather than by an independent continuous Bloch dispersion.

The nanotube electronic structure can thus be understood in terms of zone folding combined with circumferential momentum quantization. States dispersing along the nanotube axis form the 1D bands, while the transverse momentum is restricted to the values allowed by the periodic boundary condition around the circumference. Curvature and structural relaxation modify these bands quantitatively, but the characteristic spin splitting is already present in the zone-folded electronic structure of the parent 2D layer.

MATERIAL CANDIDATES AND ROBUSTNESS OF THE SELECTION RULE

The analysis presented above shows that the chiral-angle-selected spin splitting of the nanotubes is inherited from the momentum-dependent spin splitting of the parent 2D d-wave electronic structure through zone folding and circumferential quantization, subject to the symmetries that remain after rolling. An important question is whether the resulting antinodal–nodal selection rule remains robust across different material realizations, where rolling can

produce substantial structural changes and sublattice moment imbalance. We therefore extend the analysis beyond V_2O to representative symmetric and Janus systems.

The rapidly expanding family of layered and predicted monolayer altermagnets provides a broad candidate space for nanotubes and related curved low-dimensional structures. In sufficiently flexible atomically thin materials, rolling or scrolling could provide a route from a 2D parent layer to a quasi-1D geometry. Janus monolayers are of particular interest in this context because their intrinsic out-of-plane structural asymmetry provides a distinct chemical environment for examining the effects of rolling. More generally, nanotubes and nanoscrolls realized from other families of atomically thin materials demonstrate the feasibility of transforming layered systems into curved quasi-1D structures.

Several members of the layered V_2X_2O family (X = Se, Te), including KV_2Se_2O and RbV_2Te_2O, have recently been identified as layered d-wave altermagnets [4–6]. Their quasi-two-dimensional character makes them experimentally motivated parent compounds for exploring low-dimensional structures based on altermagnetic layers. These layered systems therefore provide a connection between the minimal V_2O system considered in the main text and possible material platforms for nanotubes rolled from 2D d-wave altermagnetic layers.

Beyond these experimentally motivated layered systems, recent high-throughput studies have identified a broad range of predicted monolayer altermagnets and related candidate materials spanning diverse chemical compositions and crystal structures [7, 8]. Together, these developments define a broad materials space in which the consequences of rolling 2D altermagnetic electronic structures into quasi-1D geometries can be explored.

Table S1 summarizes representative candidate monolayers selected from experimentally motivated layered altermagnetic systems and recently proposed 2D altermagnetic material families, including compounds identified in high-throughput searches for monolayer altermagnets [7]. The listed systems span Ti-, V-, Cr-, Mn-, Fe-, Co-, and Ni-based compounds. The lattice constants listed in Table S1 are taken from the DFT+U high-throughput calculations of Ref. [7]; they can therefore differ from the PBE-optimized values obtained in the present calculations and reported in Table S2. Since the magnetic and electronic properties of several of these materials can depend sensitively on the treatment of electronic correlations, Table S1 is intended to illustrate the diversity of potential parent materials rather than to provide a ranking of nanotube candidates. In particular, the inclusion of a material in Table S1 does not establish the structural stability, magnetic configuration, or electronic structure of its rolled form; these properties must be determined explicitly for each nanotube geometry.

To test the selection rule beyond V_2O, we performed explicit first-principles calculations for V_2OSe_2, V_2OSeTe, and Fe_2SSe. These systems represent distinct structural and magnetic responses to rolling: V_2OSe_2 provides a symmetric reference, V_2OSeTe is a Janus system with out-of-plane structural asymmetry, and Fe_2SSe is a Janus system that develops a substantially larger sublattice moment imbalance upon rolling. Compared with the nearly compensated V_2O nanotube discussed in the main text, these systems provide a broader range of residual magnetic moments with which to test the robustness of the antinodal–nodal distinction. Table S2 summarizes the magnetic moments as a function of nanotube radius.

For the V-based systems V_2OSe_2 and V_2OSeTe, the residual magnetic moment $\Delta M = |M_1 + M_2|$ decreases systematically with increasing nanotube radius. V_2OSe_2, for example, exhibits $\Delta M = 0.15\,\mu_B$ for $R \approx 5$ Å, decreasing

TABLE S1. Representative 2D altermagnetic monolayers considered as potential parent materials for nanotube realization. The listed materials are drawn from experimentally motivated layered altermagnetic systems and recently proposed monolayer altermagnetic families identified through computational searches [7]. Their inclusion does not imply that the corresponding nanotube structures have been established as stable. The lattice constants in parentheses are the DFT+U values reported in the corresponding high-throughput study [7].

Ti-based	V-based	Cr-based	Mn-based	Fe-based	Co-based	Ni-based
Ti_2F_2O (4.13)	V_2OSe_2 (4.03)	Cr_2OSe_2 (3.99)	Mn_2F_2O (4.06)	Fe_2Cl_2O (4.03)	Co_2Cl_2S (4.54)	Ni_2Se_2O (3.90)
Ti_2Cl_2O (4.24)	V_2OTe_2 (4.08)	Cr_2OTe_2 (4.07)	Mn_2Cl_2O (4.18)	Fe_2Br_2O (4.07)	Co_2ClBrS (4.47)	Ni_2Te_2O (3.84)
Ti_2Cl_2S (4.86)	V_2OSeTe (3.94)	Cr_2OSSe (4.54)	Mn_2Cl_2S (4.74)	Fe_2I_2O (4.12)	Co_2NPSe (4.27)	Ni_2P_2O (3.92)
Ti_2Cl_2Se (5.05)	V_2OSeS (3.94)	Cr_2OSeTe (4.29)	Mn_2Cl_2Se (4.93)	Fe_2I_2 (4.14)	Co_2NPTe (4.21)	Ni_2As_2O (3.85)
Ti_2Cl_2Te (5.38)	V_2OTeS (3.99)	Cr_2Br_2O (4.09)	Mn_2Br_2O (4.21)	Fe_2O_2 (3.49)	Co_2NAsS (4.20)	Ni_2F_2 (3.47)
Ti_2Br_2O (4.27)	V_2Br_2O (4.18)	Cr_2STeO (4.00)	Mn_2Br_2S (4.80)	Fe_2S_2 (3.80)	Co_2NAsSe (4.16)	Ni_2Cl_2 (3.64)
Ti_2Br_2S (4.91)	V_2F_2O (4.04)	Cr_2F_2O (4.00)	Mn_2OSeTe (4.62)	Fe_2Se_2 (3.92)	Co_2NAsTe (4.31)	Ni_2Br_2 (3.76)
Ti_2Br_2Se (5.15)	V_2Cl_2O (4.14)	Cr_2Cl_2O (4.07)	Mn_2OTeO (3.98)	Fe_2ClBrO (4.05)	Co_2PAsS (4.38)	Ni_2I_2 (3.97)
Ti_2Br_2Te (5.42)	V_2S_2O (3.98)	Cr_2S_2O (3.94)	Mn_2STeO (4.06)	Fe_2ClIO (4.08)	Co_2PAsSe (4.31)	Ni_2SSeO (3.88)
Ti_2I_2O (4.30)	V_2F_2 (3.81)	Cr_2Se_2 (3.94)	Mn_2S_2 (3.92)	Fe_2BrIO (4.10)	Co_2PAsTe (4.39)	Ni_2STeO (3.91)

TABLE S2. Magnetic moments of representative nanotubes rolled from V_2OSe_2, V_2OSeTe, and Fe_2SSe monolayers. The PBE-optimized lattice constant a and magnetic moments of the corresponding parent monolayers obtained in the present calculations are given for reference. For each nanotube radius, M_1 and M_2 denote the magnetic moments of the two magnetic sublattices, while $\Delta M = |M_1 + M_2|$ denotes the residual magnetic moment. All nanotubes listed have chiral angle $\theta = 0°$.

Material	2D monolayer		$R \approx 5$ Å				$R \approx 10$ Å				$R \approx 15$ Å			
	a	M_1/M_2	R	M_1	M_2	ΔM	R	M_1	M_2	ΔM	R	M_1	M_2	ΔM
	(Å)	(μ_B)	(Å)		(μ_B)		(Å)		(μ_B)		(Å)		(μ_B)	
V_2OSe_2	3.90	1.57/-1.57	4.97	1.31	-1.46	0.15	9.94	1.52	-1.56	0.04	14.91	1.55	-1.57	0.02
V_2OSeTe	3.92	1.59/-1.59	5.00	1.05	-1.40	0.35	10.0	1.42	-1.57	0.15	15.00	1.48	-1.58	0.10
Fe_2SSe	3.67	1.94/-1.94	5.19	1.06	-1.75	0.69	9.73	1.44	-1.86	0.42	14.91	1.63	-1.89	0.26

to 0.04 μ_B for $R \approx 10$ Å and 0.02 μ_B for $R \approx 15$ Å. The Janus V_2OSeTe nanotubes show the same trend but larger residual moments of 0.35, 0.15, and 0.10 μ_B, respectively. The decrease of ΔM with increasing radius is consistent with the weakening of curvature-induced inner–outer inequivalence as the nanotubes approach the large-radius limit.

Fe_2SSe nanotubes exhibit substantially larger residual moments over the investigated radius range. The smallest nanotube considered here has $\Delta M = 0.69$ μ_B, which decreases to 0.42 μ_B for $R \approx 10$ Å and 0.26 μ_B for $R \approx 15$ Å. This stronger radius dependence is consistent with a greater sensitivity of the Fe_2SSe magnetic state to rolling-induced changes in local bonding and hybridization.

The remaining question is whether these material-dependent structural and magnetic changes modify the characteristic antinodal–nodal distinction. Figure S2 compares the electronic structures of representative V_2OSeTe and Fe_2SSe nanotubes with those of the corresponding parent monolayers and unrolled rectangular supercells. For V_2OSeTe [Fig. S2(a)], the bands of the unrolled rectangular supercell along Γ–X closely resemble those of the $\theta = 0°$ antinodal nanotube along Γ–Z. This correspondence shows that the characteristic antinodal spin splitting is already present in the zone-folded electronic structure before rolling. The complete spectrum of the $\theta = 45°$ nodal nanotube remains spin degenerate, consistent with the surviving sublattice-exchanging mirror symmetry combined with spin reversal discussed in the main text.

For Fe_2SSe [Fig. S2(b)], the nanotube bands show larger quantitative deviations from those of the corresponding unrolled rectangular supercell, consistent with the stronger structural and magnetic response to rolling. Nevertheless, the characteristic antinodal–nodal distinction is preserved: the $\theta = 0°$ antinodal nanotube is spin split, whereas the complete spectrum of the $\theta = 45°$ nodal nanotube remains spin degenerate. The selection rule therefore survives even when rolling produces substantial quantitative modifications of the electronic structure.

Overall, these calculations show that material-dependent structural changes and sublattice moment imbalance can quantitatively modify the nanotube electronic structure without removing the characteristic antinodal–nodal distinction. The antinodal spin splitting is already encoded in the zone-folded electronic structure of the parent 2D layer, whereas the nodal spin degeneracy is protected by the sublattice-exchanging mirror symmetry combined with spin reversal that survives rolling. The chiral-angle-selected spin splitting established in the main text is therefore robust across the representative symmetric and Janus nanotube systems considered here.

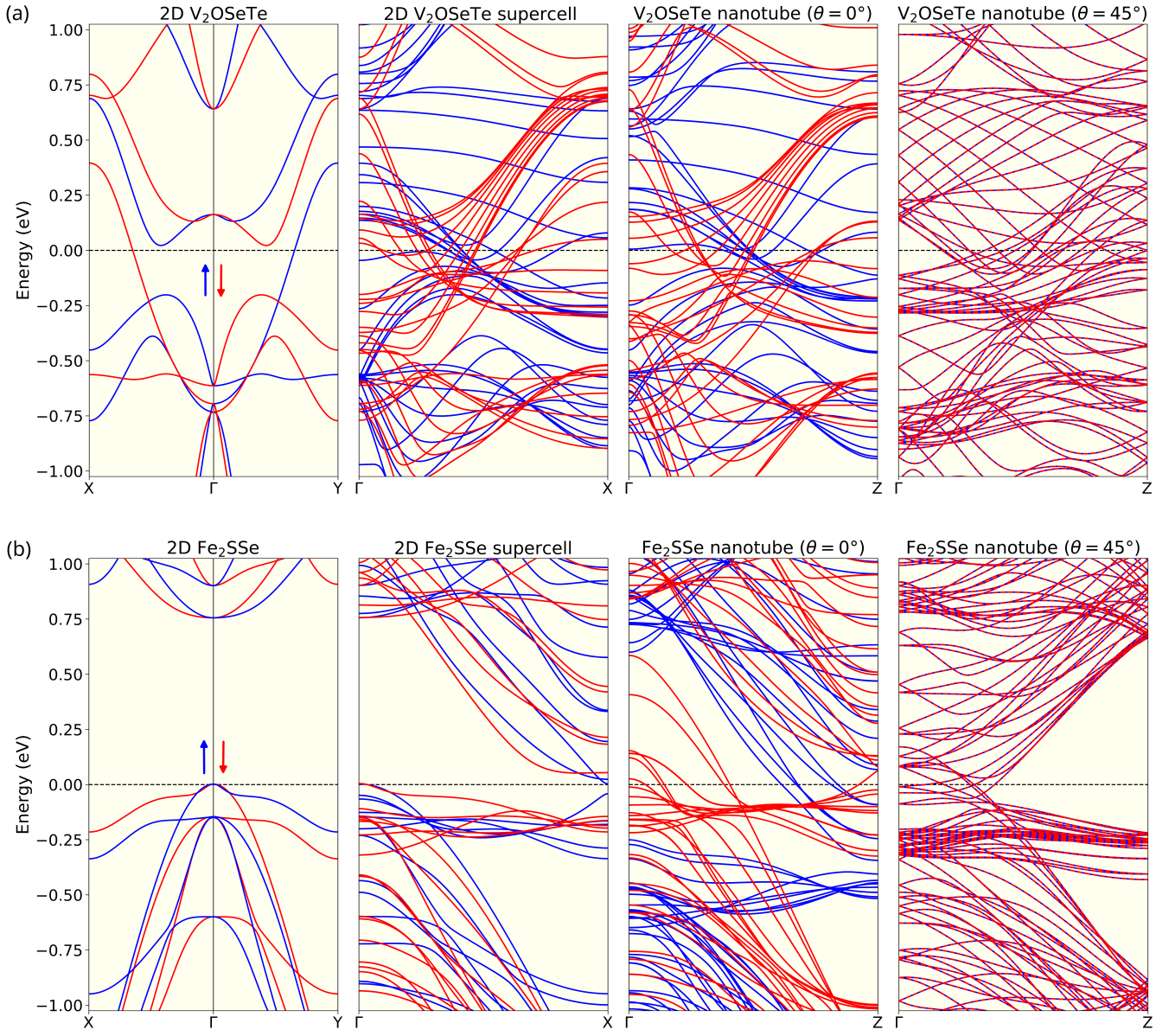


FIG. S2. Spin splitting in representative Janus nanotubes. (a) Evolution of the electronic structure of V_2OSeTe from the parent 2D monolayer to the corresponding nanotube states. From left to right: band structure of the parent 2D monolayer along X–Γ–Y, zone-folded band structure of the unrolled rectangular supercell along Γ–X, and nanotube band structures for chiral angles $\theta = 0°$ and $\theta = 45°$ calculated along the nanotube axis Γ–Z. The nanotube radius is $R \simeq 10$ Å. (b) Same as in (a), but for Fe_2SSe with $R \simeq 10$ Å. In both systems, the antinodal $\theta = 0°$ nanotube is spin split, whereas the complete spectrum of the nodal $\theta = 45°$ nanotube remains spin degenerate. Quantitative deviations between the unrolled-supercell and nanotube bands are larger for Fe_2SSe, but the antinodal–nodal distinction is preserved.

[1] S. Smidstrup, T. Markussen, P. Vancraeyveld, J. Wellendorff, J. Schneider, T. Gunst, B. Verstichel, D. Stradi, P. A. Khomyakov, U. G. Vej-Hansen, M.-E. Lee, S. T. Chill, F. Rasmussen, G. Penazzi, F. Corsetti, A. Ojanperä, K. Jensen, M. L. N. Palsgaard, U. Martinez, A. Blom, M. Brandbyge, and K. Stokbro, J. Phys.: Condens. Matter **32**, 015901 (2019).
[2] J. P. Perdew, K. Burke, and M. Ernzerhof, Phys. Rev. Lett. **77**, 3865 (1996).
[3] M. J. Van Setten, M. Giantomassi, E. Bousquet, M. J. Verstraete, D. R. Hamann, X. Gonze, and G.-M. Rignanese, Comput. Phys. Commun. **226**, 39 (2018).
[4] B. Jiang, M. Hu, J. Bai, Z. Song, C. Mu, G. Qu, W. Li, W. Zhu, H. Pi, Z. Wei, Y. Sun, Y. Huang, X. Zheng, Y. Peng, L. He, S. Li, J. Luo, Z. Li, G. Chen, H. Li, H. Weng, and T. Qian, Nature Physics **21**, 754 (2025).
[5] A. Ablimit, Y.-J. Sun, H. Jiang, C. Wu, L. Wei, X. Chen, and G. Cao, Physical Review Materials **2**, 044801 (2018).
[6] X. Cheng, Y. Gao, J. Peng, and J. Liu, arXiv (2026), arXiv:2602.09465 [cond-mat.mtrl-sci].
[7] R. Xu, Y. Gao, and J. Liu, National Science Review **13**, nwaf528 (2026).
[8] A. González-García, W. López-Pérez, P. Pacheco, L. Ramírez-Montes, and R. González-Hernández, Physical Review Materials **10**, 044004 (2026).